Int J Fract (2016) 201:97–118
DOI 10.1007/s10704-016-0125-7

ORIGINAL PAPER

A comparative study of the r-adaptive material force approach and the phase-field method in dynamic fracture

Christian Steinke · Kaan Özenç · Gor Chinaryan · Michael Kaliske

Received: 28 July 2015 / Accepted: 26 May 2016 / Published online: 17 June 2016

Abstract This contribution presents a comparison between a discrete and a smeared approach to approximate a crack in finite element simulations including the contribution of inertia to the behavior of brittle material under transient loading in the case of fracture. The discrete approximation of a crack is based in this case on a node duplication technique triggered by the evaluation of the so-called "material force" at the crack tip. The smeared approximation of a crack bases on the diffuse description of the crack by a phase-field approach. The governing equations under consideration of transient contributions are shown and the procedure for the finite element implementation is outlined. Numerical simulations investigate the capabilities and limitations of both methods. Firstly, the procedure to introduce initial cracks in a structure and the setup necessary to make them interact with stress waves properly, are under investigation. Moreover, this study deals with the evaluation of the velocity of the crack propagation and its comparison to experimental data. Finally, the phenomenon of crack branching is studied. The presentation and discussion of the results of the simulations provide an overview on the potential of both approaches with respect to an efficient and a realistic simulation of fracture processes in dynamic problems.

C. Steinke · K. Özenç · G. Chinaryan · M. Kaliske (✉)
Institute for Structural Analysis, Technische Universität, Dresden, Germany
e-mail: Michael.Kaliske@tu-dresden.de

Keywords Dynamic fracture · Material force · Phase-field · Wave propagation · Crack propagation velocity · Crack branching

1 Introduction

The theory of fracture mechanics addresses the physical background of the formation and propagation of cracks. Much effort has been put to understand and to clarify the mechanisms of fracture in various kinds of materials and presumptions since the considerations on brittle fracture in solids in the early 1920s. The first step towards a comprehensive theory of fracture mechanics, published in Griffith (1921), was the interpretation of the resistance against crack propagation in a material as an effect of a material property that describes the amount of energy to be dissipated via the creation of new surfaces inside the material. The source of the energy required for dissipation is expected to be the strain energy that is stored in the deformation of the immediate vicinity of the crack tip. The concept of the J-Integral, presented in Rice (1968), enables the determination of the "crack driving force" in an elastic solid. The relation between the J-Integral and the theory of "material forces" is presented in the books Gurtin (2000), Kienzler and Herrmann (2000) and Maugin (2010). The finite element implementation of material forces and the simulation of classical examples of fracture mechanics are outlined in Braun (1997), Müller and Maugin (2002) and Stein-

mann (2000). Moreover, the thermodynamical consistency of the approach within a theory of brittle fracture in elastic solids is shown by Gürses and Miehe (2009) and Miehe and Gürses (2007). In the work of Maugin and Trimarco (1992), the theory is developed within the context of large strain. Unfortunately, most of the studies are confined to an elastic material response, although the scenario related to energy dissipations seems to be quite predictable in this case. In case of plasticity, the material force approach has been discussed by Menzel et al. (2004), Özenç et al. (2014) and Simha et al. (2008). The extension to nonlinear and inelastic materials in case of viscoelasticity is treated by Näser et al. (2009). Moreover, the theory of material forces always requires a pre-existing crack to evaluate the behavior of the crack at specific loads. The initiation of the crack requires additional assumptions.

Another approach emerged recently within the work of Bourdin (2007, 2008), Francfort and Marigo (1998) and Karma et al. (2001). The questions with respect to crack initiation, propagation, branching and arrest are answered by variational principles based on energy minimization. The additional field parameter "phase-field" is introduced and interpreted as the regularized approximation of the crack. The relation of the surface energy to the regularized size of the surface of the crack allows the consideration of an additional dissipative contribution in a general energetic description of the problem. The implementation into a finite element framework is independently shown and applied to standard brittle fracture examples in Hofacker et al. (2009) and Kuhn and Müller (2010). Also, the simulation of the phenomenon of crack branching is possible by extending the energetic equilibrium to the dynamic case, see e.g. Borden (2012). In this respect, the paper at hand contributes to recent research.

All experimental verification examples include inertia effects with considerable influence on the outcome and it is hardly possible to imagine an experimental setup to investigate the nucleation and the propagation of cracks where the transient effects are insignificant. Therefore, a model neglecting the impact of inertia is always insufficient to capture real life fracture examples. Thus, their introduction is an essential component of a comprehensive approach to fracture that is able to deliver insight for structural design where the phenomenon of fracture is relevant. In this paper, a dynamic material force approach and a dynamic phase-field approach are applied to general dynamic model problems as well as experimental examples in order to show the general features, benefits and drawbacks of the theories. Based on these results, further research topics are outlined.

In the first section of this study, a compact insight into the relevant assumptions and derivations necessary, in order to implement the phase-field approach and the material force approach into a finite element framework, is given and also detailed references for further information are provided. Furthermore, the post processing of the results provided by the smeared crack approximation is discussed. The second section contains the application of both methods to theoretical and experimental examples of fracture mechanics. The first example models a simple structure with a pre-existing crack at transient loading. The structural response in form of wave propagation and the wave's interaction with the pre-existing crack are simulated and discussed. The second example presents an experimentally verified crack propagation problem provided in Sharon et al. (1996) and a detailed discussion of the results. The third problem and the fourth example are theoretical benchmarks, where a structure with a pre-existing crack is subjected to shock loading in such a way, that crack propagation and branching are enforced. Concluding remarks and comments close the paper.

2 Numerical approaches to dynamic fracture

2.1 Numerical approximation of fracture

Whenever fracture processes are simulated by finite element computations, the appropriate method to model and represent the crack itself has to be choosen. Two general classes are available, namely the smeared and the discrete approach to model a crack.

The material force formulation belongs to the discrete crack approximation, representing the crack by discrete edges of the mesh. Any crack propagation requires the adaptation of the mesh by duplication of nodes and updated element connectivities. The material force approach can obtain straight propagation and kinking of cracks in a straight forward manner. Additional effort has to be put into the formulation for the simulation of the branching phenomena.

The phase-field approach falls into the class of the smeared crack approximation. As already mentioned, the crack is realized by its regularized approximation

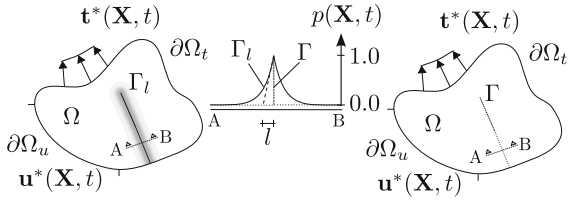

Fig. 1 Continuum Ω with sharp crack Γ and smeared crack approximation Γ_l

through the phase-field as an additional field variable of the continuum that affects the relation of strains and stresses. The inclusion of the dissipative energetic contribution of the crack's surface in the global energy balance equation makes it possible to simulate all relevant aspects of fracture, i.e. nucleation, propagation, arrest and branching without further assumptions.

2.2 Energetic description of dynamic brittle fracture

The following subsections present the mathematical formulations of the discrete and the smeared approaches in the context of an energetic description of brittle fracture under consideration of dynamic phenomena. Furthermore, the different ways of both approaches to model crack nucleation and propagation are described and compared.

2.2.1 Phase-field approach

The phase-field approach is a recently developed smeared approach to numerical crack approximation. A comprehensive overview on the existing formulations is given e.g. in Ambati et al. (2015).

A body Ω as depicted in Fig. 1 is considered. It is restricted by the outer boundary $\partial\Omega$ and contains the crack Γ. The boundary $\partial\Omega$ consists of two parts, where $\partial\Omega_u$ is the portion with prescribed displacements $\mathbf{u}^*(\mathbf{X},t)$ and $\partial\Omega_t$ is the part with prescribed stresses $\mathbf{t}^*(\mathbf{X},t)$. Inside the body, the field variables for the displacement, velocity and acceleration are defined with respect to space and time by $\mathbf{u}(\mathbf{X},t)$, $\dot{\mathbf{u}}(\mathbf{X},t)$ and $\ddot{\mathbf{u}}(\mathbf{X},t)$, respectively. In addition, a continuous scalar phase-field $p(\mathbf{X},t)$ is introduced as a parameter to distinguish the unbroken ($p=0$) from the broken phase ($p=1$) of the material. The transition zone between broken and unbroken material is characterized by the regularization length l. According to the theory of Γ-convergence, explained in Braides (2002), the sharp crack is approximated in the limiting case of $l \to 0$.

The strong form of the dynamic phase-field model for brittle fracture is derived out of a HAMILTONIAN principle. A detailed description of the procedure is given by Schlüter et al. (2014). The HAMILTONIAN principle reads in general

$$\delta \int_{t_1}^{t_2} \int_{\Omega} \mathcal{L}\, dV + \int_{\partial\Omega} \mathbf{t}^* \cdot \mathbf{u}\, dA\, dt = 0. \tag{1}$$

The LAGRANGIAN density $\mathcal{L}$ considers the energetic contributions of the kinetic energy ψ_{kin}, the strain energy ψ_{eps} and the dissipated energy ψ_{dis} by

$$\mathcal{L} = \psi_{kin} - \psi_{eps} - \psi_{dis}. \tag{2}$$

The kinetic energy density is defined as

$$\psi_{kin} = \frac{1}{2}\,\rho\,\dot{\mathbf{u}}\cdot\dot{\mathbf{u}}. \tag{3}$$

The strain energy density is based on the HELMHOLTZ energy density for a linear elastic material as

$$\psi_{lin} = \frac{\lambda}{2}\,(\boldsymbol{\varepsilon}\colon\mathbf{1})^2 + \mu\,\boldsymbol{\varepsilon}^2\colon\mathbf{1}. \tag{4}$$

According to GRIFFITH's theory given in Griffith (1921), the propagation of a crack dissipates strain energy into the formation of new surfaces. Two approaches define the portion of the strain energy density ψ^+ related to crack formation in

$$\psi_{lin} = \psi^+ + \psi^-. \tag{5}$$

The first one is the split into volumetric and deviatoric components presented by Amor et al. (2009) and is only mentioned for the sake of completeness. This study focuses on the second approach that is introduced by Miehe et al. (2010a, b). MIEHE proposes a spectral decomposition of the strain tensor $\boldsymbol{\varepsilon}$ into principal strains by

$$\begin{aligned}\boldsymbol{\varepsilon} &= \boldsymbol{\varepsilon}^+ + \boldsymbol{\varepsilon}^- \\ &= \sum_i \langle\varepsilon_i\rangle_+\,\mathbf{n}_i\otimes\mathbf{n}_i + \sum_i \langle\varepsilon_i\rangle_-\,\mathbf{n}_i\otimes\mathbf{n}_i.\end{aligned} \tag{6}$$

The principal strains are formulated by eigenvalues ε_i and eigenvectors $\mathbf{n}_i$. With the bracket operators $\langle x\rangle_+ = \frac{x+|x|}{2}$ and $\langle x\rangle_- = \frac{x-|x|}{2}$, they are assigned to tensile and compressive contributions, $\boldsymbol{\varepsilon}^+$ and $\boldsymbol{\varepsilon}^-$, respectively. The decomposed linear elastic strain energy density reads

$$\psi_{lin} = \underbrace{\frac{\lambda}{2}\,\langle \boldsymbol{\varepsilon} : \mathbf{1}\rangle_+{}^2 + \mu\,\boldsymbol{\varepsilon}^{+2} : \mathbf{1}}_{\psi^+} + \underbrace{\frac{\lambda}{2}\,\langle \boldsymbol{\varepsilon} : \mathbf{1}\rangle_-{}^2 + \mu\,\boldsymbol{\varepsilon}^{-2} : \mathbf{1}}_{\psi^-}. \tag{7}$$

As the phase-field reaches the fully broken state at $p = 1$, the part of the strain energy density ψ^+ is degraded in analogy to damage formulations by the function

$$g(p) = (1-p)^2 + \eta \tag{8}$$

with the residual stiffness coefficient η. The relation between the phase-field and the portion of the strain energy density ψ^+ assigned to crack formation defines the modified strain energy density of Eq. (2) by

$$\psi_{eps} = g(p)\,\psi^+ + \psi^-. \tag{9}$$

Based on the modified strain energy density, also the stresses are decomposed into compressive and degraded tensile contributions by

$$\boldsymbol{\sigma} = \frac{\partial \psi_{eps}}{\partial \boldsymbol{\varepsilon}} = \underbrace{g(p)\,\frac{\partial \psi^+}{\partial \boldsymbol{\varepsilon}}}_{\boldsymbol{\sigma}^+} + \underbrace{\frac{\partial \psi^-}{\partial \boldsymbol{\varepsilon}}}_{\boldsymbol{\sigma}^-}. \tag{10}$$

The dissipated energy density is based on the regularized crack surface

$$\Gamma_l = \int_\Omega \frac{1}{2l}\left(p^2 + l^2\,|\nabla p|^2\right) dV. \tag{11}$$

The multiplication of the crack's surface with the fracture toughness $\mathcal{G}_c$ yields the dissipated energy. Thus, the dissipated energy density reads

$$\psi_{dis} = \frac{\mathcal{G}_c}{2l}\left(p^2 + l^2\,|\nabla p|^2\right). \tag{12}$$

A detailed description of the steps that are necessary to obtain the strong form out of the HAMILTONIAN principle is given in Schlüter et al. (2014). Following these steps considering above definitions, the strong form of the dynamic phase-field is

$$\rho\,\ddot{\mathbf{u}} - \operatorname{div}\boldsymbol{\sigma} = 0 \tag{13}$$

and

$$2\,(1-p)\,\psi^+ - \frac{\mathcal{G}_c}{l}p + \mathcal{G}_c\,l\,\nabla^2 p = 0. \tag{14}$$

A macroscopic crack is irreversible in nature. Two fundamental approaches, to ensure irreversibility in the phase-field description, are available. The first model, which is outlined by Kuhn and Müller (2011), imposes additional boundary conditions on the phase-field once it reaches the "fully broken state". This allows local healing of the crack as long as the phase-field does not reach a value representing the fully broken state. Especially in dynamic calculations, with perpetual local loading and unloading, this may underestimate the energetic contributions to the crack propagation. Therefore, this study focuses on the irreversibility approach implemented by Hofacker (2013). There, it is pointed out that the evolution of the phase-field, governed by Eq. (14), is driven by the value of ψ^+. Thus, to ensure $\dot{p} \geq 0$ locally, ψ^+ at time t_i is replaced by the history variable

$$\mathcal{H}(t_i) = \max_{t\,\in\,0\ldots t_i} \psi^+(t). \tag{15}$$

A correspondent modification of Eq. (14) is

$$\frac{\mathcal{G}_c}{l}p - \mathcal{G}_c\,l\,\nabla^2 p = 2\,(1-p)\,\mathcal{H}. \tag{16}$$

2.2.2 Material force approach

The material force approach has been successfully used for the formulation of a thermodynamically consistent crack driving force in fracture mechanics with different frameworks for crack propagation prediction, see Brouzoulis et al. (2010), Gürses and Miehe (2009), Miehe and Gürses (2007) and Schütte (2009), but these studies are restricted to elastic small strain theory. In Özenç and Kaliske (2014), the material force based crack propagation algorithm is used for hyperelastic and viscoelastic material. However, all these studies are conducted without considering inertia forces. In case of dynamic fracturing with inertia effect, the material force approach is discussed in Özenç (2016). The implementation of the approach is based on derivations from the material momentum balance equation and the application of an implicit fracture algorithm.

The local form of the material momentum balance in the reference configuration is given as

$$\nabla_{\mathbf{X}} \cdot \boldsymbol{\Sigma} = \boldsymbol{h}^T \boldsymbol{b}_0 - \underbrace{\rho \boldsymbol{h}^T \ddot{\mathbf{u}} - \rho \dot{\boldsymbol{h}}^T \dot{\mathbf{u}}}_{\rho \frac{\partial \boldsymbol{\mathcal{P}}}{\partial t}} - \frac{1}{2}\dot{\mathbf{u}} \cdot \dot{\mathbf{u}} \nabla_{\mathbf{X}} \rho + \left.\frac{\partial \psi_{lin}}{\partial \boldsymbol{X}}\right|_{exp} \tag{17}$$

in a small strain formulation, considering $\boldsymbol{h} = \nabla_{\mathbf{X}} \boldsymbol{u}^T$. The above equation involves the material gradient

$\nabla_{\mathbf{X}}(\bullet)$, the material divergence operator $\nabla_{\mathbf{X}} \cdot (\bullet)$ and the ESHELBY stress tensor $\boldsymbol{\Sigma}$, which is also defined as $\boldsymbol{\Sigma} = -\mathcal{L}\mathbf{1} - \boldsymbol{h}^T \boldsymbol{\sigma}$ with the LAGRANGIAN density $\mathcal{L}$ specified in Eq. (2) without the dissipated energy density due to phase-field ψ_{dis} and the CAUCHY stress tensor $\boldsymbol{\sigma} = \partial_{\boldsymbol{\varepsilon}} \psi_{lin}$. Furthermore, the transpose of the gradients of the displacements $\boldsymbol{h}^T$, its partial derivative with respect to time $\dot{\boldsymbol{h}}^T$, the body forces $\boldsymbol{b}_0$, the density ρ and the free HELMHOLTZ energy density ψ_{lin} are required. In addition, the material pseudo-momentum $\boldsymbol{\mathcal{P}}$ is specified by $\boldsymbol{\mathcal{P}} = \rho \boldsymbol{h}^t \dot{\mathbf{u}}$. Here, it is useful to establish configurational volume forces

$$\boldsymbol{B} = \boldsymbol{h}^T \boldsymbol{b}_0 - \rho \overline{\dot{\boldsymbol{h}}^T \dot{\mathbf{u}}} - \frac{1}{2} \dot{\mathbf{u}} \cdot \dot{\mathbf{u}} \nabla_{\mathbf{X}} \rho - \frac{\partial \psi}{\partial \boldsymbol{X}}\Big|_{exp}. \tag{18}$$

With the surface normal $\boldsymbol{n}$, the configurational traction is defined by $\boldsymbol{T}_0 = \boldsymbol{\Sigma} \boldsymbol{n}$. After the element wise discretization of the virtual displacements, nodal based material forces $\mathcal{F}$ are obtained by a loop over the elements by

$$\mathcal{F} = \prod_{e=1}^{numel} \int_{\Omega} (\boldsymbol{\Sigma} : \nabla_{\mathbf{X}} \boldsymbol{N} + \boldsymbol{B}\boldsymbol{N})\, dV - \prod_{e=1}^{numsur} \int_{\partial\Omega} (\boldsymbol{\Sigma}\boldsymbol{n})\boldsymbol{N} dS, \tag{19}$$

with $\boldsymbol{N}$ being the shape functions of the elements. The generalized material force $\mathcal{F}$ is energy-conjugate to the thermodynamical driving force and decomposes additively into contributions for the ESHELBY stress tensor, the body forces and the surface forces, $\mathcal{F}^{\boldsymbol{\Sigma}}$, $\mathcal{F}^{body}$ and $\mathcal{F}^{sur}$, respectively, by

$$\mathcal{F} = \mathcal{F}^{\boldsymbol{\Sigma}} + \mathcal{F}^{body} + \mathcal{F}^{sur}, \tag{20}$$

where

$$\mathcal{F}^{\boldsymbol{\Sigma}} = \prod_{e=1}^{numel} \int_{\Omega} (\boldsymbol{\Sigma} : \nabla_{\mathbf{X}} \boldsymbol{N})\, dV, \tag{21}$$

$$\mathcal{F}^{body} = \prod_{e=1}^{numel} \int_{\Omega} \boldsymbol{B}\boldsymbol{N} dV \tag{22}$$

and

$$\mathcal{F}^{sur} = - \prod_{e=1}^{numsur} \int_{\partial\Omega} \boldsymbol{T}_0 \boldsymbol{N} dS. \tag{23}$$

Figure 2 illustrates a general scenario of a kinking crack. When the crack driving force reaches the critical value, the crack seeks a path of least resistance (or the path of maximum driving force) and propagates in this direction. In case of the energy minimization ansatz, the propagation follows the path in such a way that the crack driving force is maximized and the potential energy of the entire structure Π_i is minimized. The introduction of the general framework in the mathematical description yields

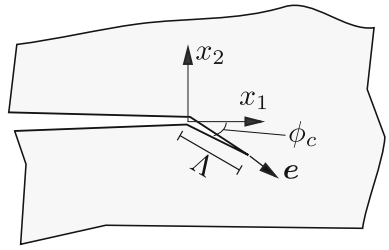

Fig. 2 Schematic view of the crack tip kink at mixed mode loading

$$\Pi_i(a + \Lambda, t) = \Pi_i(a, t) + \mathcal{F} \cdot \Lambda \boldsymbol{e} \rightarrow \text{minimum!}, \tag{24}$$

where $\boldsymbol{e} := \boldsymbol{e}(\Lambda, \phi_c)$ is the crack direction vector as shown in Fig. 2, ϕ_c is the angle between crack kinking direction and the crack surface and Λ is the incremental size of the crack. The argument yields

$$\phi_c{}^* = \arg \left\{ \inf_{\phi_c \in \left[-\frac{\pi}{2}, \frac{\pi}{2}\right]} (\Pi_i(a + \Lambda, t)) \right\}, \tag{25}$$

with $\mathcal{F} = \mathcal{F}(a, t)$. Thus, the time integration of Eq. 25 using the (implicit) backward EULER scheme yields

$$\phi_c{}^* := \arg \left\{ \inf_{\phi_c \in \left[-\frac{\pi}{2}, \frac{\pi}{2}\right]} (\Pi_i(a + \Lambda, t)) \right\} \tag{26}$$

with $\mathcal{F} = \mathcal{F}(a + \Lambda, t)$, where $\boldsymbol{e}$ is unknown and has to be found by iteration. Since, in this theory, the directions of $\mathcal{F}(a + \Lambda, t)$ and $\boldsymbol{e}$ coincide, the non-tangential component of the material force vector vanishes. Therefore, this algorithm requires an additional iterative procedure as discussed in Özenç (2016).

2.2.3 Crack evolution

The outlined derivations provide the energetic framework to model crack evolution in finite element simulations for both the smeared and the discrete approach. Crack evolution comprehends all processes related to fracture and may be divided into the two main categories nucleation and propagation.

The nucleation or initiation of cracks is restricted to the formation of a new crack in the bulk material of a structure without defects. In the phase-field approach, the nucleation is covered by the association of crack formation to the dissipation of inner energy. This is especially beneficial for transient simulations, where the propagation of the load by stress waves leads to crack initiation in the bulk material. The calculation of a material force requires a singularity or defect in the structure. In order to model the formation of a crack inside the bulk of a structure, additional assumptions are necessary. Investigations of crack nucleation are not discussed in this paper.

The propagation of cracks covers the wide range of phenomena observed for already existing cracks. A crack will advance or arrest according to the amount of energy in the immediate vicinity of the crack tip, that is available for the formation of new crack surfaces. The straight or the kinked propagation of the crack will dissipate different amounts of energy. Furthermore, the phenomenon of branching can be reviewed as the formation of two or more cracks, originating from a single crack tip. The particular behavior of the crack is governed by the principle of energy minimization. Therefore, fracture processes always lead to crack configurations that represent the energetically most beneficial structure. The only restriction is, that the path from one configuration into another does not include intermediate steps which violate the principle of energy minimization. While this is insured by the transient step by step simulation of the fracture processes, the smeared and the discrete approaches have different methods to obtain crack propagation in each of these simulation steps.

The material force approach is post-processing the mechanical fields of the finite element solution in order to calculate the material forces at the crack tip nodes. In a static simulation, the propagation of the crack is realized for every material force that exceeds the instantaneous fracture toughness $\mathcal{G}_c$. Dynamic crack propagation has been investigated experimentally by Arakawa and Takahashi (1991), Bergkvist (1974), Dally (1979), Kobayashi and Mall (1978) and Ravi-Chandar and Knauss (1984). The investigations provide a relationship between the instantaneous fracture toughness and the velocity of the macroscopic crack propagation. Figure 17 presents the results of a study on polymethyl methacrylate (PMMA). The data suggests that, while ${\mathcal{G}_c}^{dyn}$ is roughly independent of the crack propagation velocity at low propagation speed, it increases rapidly with an increasing propagation speed due to micro cracking around the macro crack. Therefore, a generic form for the functional dependence of ${\mathcal{G}_c}^{dyn}$ is introduced by

$$ {\mathcal{G}_c}^{dyn} = \mathcal{G}_c \left(1 - \left(\frac{v_{cmf}}{v_{lim}} \right)^{\alpha} \right)^{-1} . \tag{27} $$

v_{cmf} is the crack propagation velocity, v_{lim} and α are model parameters. The simulation of the phenomenon of branching requires an additional criterion to define the circumstances necessary to trigger branching. A general approach is employed in Ramulu and Kobayashi (1985) and Kobayashi et al. (1972) and defines the value

$$ {\mathcal{G}_c}^{branch} = m \cdot \mathcal{G}_c \tag{28} $$

to be the energy release rate necessary to initiate a bifurcation of the crack. Here, the factor m is a constant multiplier for the critical energy release rate which is generally larger than 2.

In the phase-field approach, the crack is approximated by the phase-field as an additional degree of freedom. The energetic contribution of the crack formation is covered by the additional differential Eq. (14), that has to be fulfilled for each time step. The resulting phase-field represents the energetically most beneficial crack configuration and covers straight propagation, kinking and branching in a straight forward manner. The calculation of the velocity of crack propagation requires the identification of the crack tip. This identification and the evaluation of the crack propagation velocity is part of the investigations of this paper for the phase-field approach and, therefore, the implementation of the relation between the fracture toughness ${\mathcal{G}_c}^{dyn}$ and the crack propagation velocity v_{cmf} is omitted. Furthermore, there is no additional branching criterion required. Every crack branching in the phase-field method directly originates out of the global energetic description of the problem and provides the energetically most beneficial branched crack configuration possible.

2.3 Algorithmic aspects of fracture simulation

The simulation of both, the smeared and the discrete approach to dynamic fracture, requires the solution of the balance equations with respect to time. In the

phase-field approach, this solution yields, on the one hand, increments for the kinematic fields to describe the motion and deformation under load and, on the other hand, increments for the phase-field, which is representing the crack pattern. In the material force approach, the solution of the balance equations yields only increments for the kinematic fields and a post-processing step is necessary, in order to calculate material forces. Then, the crack propagation criteria are checked in order to identify critical nodes and realize the crack propagation where necessary. In both approaches, the evaluation of the crack propagation velocity is an important part of the analysis of fracture simulations. The evaluation requires the identification of the crack tip and its tracking.

The following subsections present insight into the solution of the balance equation with respect to transient contributions and the algorithmic aspects of the realisation of crack propagation for the material force approach. Furthermore, information on the crack tip identification and the evaluation of the crack propagation velocity are presented for both approaches.

2.3.1 Dynamic field solution

Nonlinear dynamic responses of FE structures are governed by

$$\mathbf{S} \cdot \Delta\mathbf{d} = \Delta\mathbf{R}. \tag{29}$$

This equation comprehends the description of the change of the field variables $\Delta\mathbf{d}$ from time t_n to t_{n+1} for all nodes of the spatial discretization of the system by a finite element meshing. The assembling procedure of the element contribution to the global equation system is implemented in a standard way and is not addressed in this paper. Within the time increment $\Delta t = t_{n+1} - t_n$, the vector of the increments of nodal forces

$$\Delta\mathbf{R} = \mathbf{R}(t_{n+1}) - \mathbf{R}(t_n) \tag{30}$$

is balanced with the multiplication of the tangent

$$\mathbf{S} = c_1\,\mathbf{K} + c_2\,\mathbf{D} + c_3\,\mathbf{M} \tag{31}$$

and the vector of increments for the nodal degrees of freedom

$$\Delta\mathbf{d} = \mathbf{d}(t_{n+1}) - \mathbf{d}(t_n). \tag{32}$$

In the material force approach, the vector of the nodal degrees of freedom $\mathbf{d}$ only contains the displacement fields. In the phase-field approach, the phase-field is additionally included in the vector of the nodal degrees of freedom. The tangent $\mathbf{S}$ consists of contributions for mass, damping and stiffness, $\mathbf{M}$, $\mathbf{D}$ and $\mathbf{K}$, respectively. While mass, damping and stiffness are directly related to displacement, velocity and accelaration in respect of the kinematic fields, there is no mass, damping or stiffness in the strict sense for the phase-field approach. Instead, everything, that affects the increment of the phase-field directly, belongs to the stiffness matrix. The damping and mass contributions affect the rate of the phase-field and the second derivative of the phase-field with respect to the time, respectively. In the formulation presented in this paper, there is only stiffness contribution for the phase-field degree of freedom. The notation in Eq. (31) decouples time from material and spatial discretization by using scalar multipliers c_1, c_2 and c_3 only depending on the choice of the time step integration method, i.e. the finite difference discretization in time.

In this study, two time integration methods are applied. The first one is the standard implicit NEWMARK time integration with two parameters $\beta = 0.25$ and $\gamma = 0.5$. Corresponding, the tangent multipliers are

$$\begin{aligned} c_1 &= 1, \\ c_2 &= \tfrac{\gamma}{\beta\,\Delta t} \quad \left(= \tfrac{2}{\Delta t}\right) \quad \text{and} \\ c_3 &= \tfrac{1}{\beta\,\Delta t^2} \quad \left(= \tfrac{4}{\Delta t^2}\right). \end{aligned} \tag{33}$$

The second approach is the HHT time integration method as described in Hilber et al. (1977). It basically damps out high frequency responses while leaving low frequency results as unaffected as possible. It is controlled by a single parameter α which is set to $\alpha = 0.667$ as proposed in Borden (2012). Thus, the tangent multipliers become

$$\begin{aligned} c_1 &= \alpha \qquad\qquad (= 0.667)\,, \\ c_2 &= \tfrac{4\,\alpha\,\left(\frac{3}{2}-\alpha\right)}{(2-\alpha)^2\,\Delta t} \quad \left(= \tfrac{1.25075}{\Delta t}\right) \quad \text{and} \\ c_3 &= \tfrac{4}{(2-\alpha)^2\,\Delta t^2} \quad \left(= \tfrac{2.25113}{\Delta t^2}\right). \end{aligned} \tag{34}$$

It has been pointed out in Kuhn and Müller (2011) and Miehe et al. (2010b) that there should not be a

full degradation of the element stiffness in the broken state of the phase-field. This is ensured by the small residual stiffness coefficient $\eta \ll 1$ in Eq. (8). Furthermore, a staggered solution scheme has been developed in Hofacker et al. (2009). Both, the residual stiffness coefficient and the staggered scheme are applied for numerical fracture analysis in static simulations. In the static case, the tangent $\mathbf{S}$ is restricted to stiffness contributions. Therefore, the total degradation of certain element stiffness matrices results in a singular global tangent in static simulations and renders the solution impossible. The inertia contribution to the global tangent in dynamic simulation is not affected by the degradation due to the phase-field and, therefore, stabilizes the solution in these cases. For this reason, $\eta = 0$ is applied in all simulations of this paper. Furthermore, the stabilization by the inertia allows the application of a monolithic solution scheme for all kind of fracture problems.

2.3.2 R-adaptivity

The algorithmic treatment of the implicit material force method described in Eq. (26) is briefly introduced here. At first, the data structure is introduced in an object-oriented scheme. Similar to the studies of Miehe and Gürses (2007), Ortiz and Pandolfi (1999) and Pandolfi and Ortiz (2002), a two-dimensional triangle element $\mathfrak{s}$ is introduced as an object composed of three nodes $\{\mathfrak{n}_i\}_{i=1\ldots3}$, and three lines $\{\mathfrak{l}_i\}_{i=1\ldots3}$, where a line $\mathfrak{l}$ is also an object and consists of two nodes $\{\mathfrak{n}_i\}_{i=1\ldots2}$, as shown in Fig. 3.

After creating objects for the data structure, the next step is the computation of the configurational force vector $\mathcal{F}_n$ at all nodal points of the finite element mesh. After that, the critical node $\mathfrak{n}_c$ is determined by a loop over the crack tip nodes of the finite element mesh to find the ones having the tangential component of the material force vector larger than the critical value $\mathcal{G}_c$. $\mathfrak{n}_c$ describes the crack tip, where a possible advancement of the crack may take place, as shown in Fig. 4. After having found $\mathfrak{n}_c$, the critical line $\mathfrak{l}_c$ has to be determined. This is done by another loop over the line elements connected to the critical node $\mathfrak{n}_c$. The loop is carried out over the line elements $\mathfrak{l}_c$, where the dot product of the material force vector and the normal of the line element $\boldsymbol{n}_{\mathfrak{l}}$ is the minimum compared to the other elements as

$$\mathfrak{l}_c := \arg\left\{ \inf_{\mathfrak{l}=1\ldots num_{\mathfrak{l}}} (|\mathcal{F}_n \cdot \boldsymbol{n}_{\mathfrak{l}}|) \right\}. \tag{35}$$

Then, for r-adaptation, the node $\mathfrak{n}_{tip}$ should be moved to the position where $\boldsymbol{n}_{\mathfrak{l}_c}$ becomes perpendicular to the new material force vector $\mathcal{F}_{n+1}$. $\mathcal{F}_{n+1}$ is the material force vector at the next crack tip position of the new crack tip node $\mathfrak{n}_{tip}$ at frozen time as the last step of the algorithm as shown in Fig. 4. It is important to note that obtaining $\mathcal{F}_{n+1}$ requires one more solution after the structure changes. To find the maximum crack driving force direction, another inner product function, where the normal vector and the just obtained material force vector are minimized, is introduced by

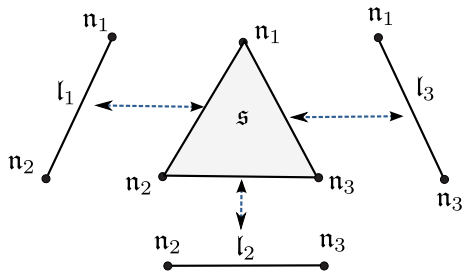

Fig. 3 Schematic view of the data structure of a *triangle* surface element

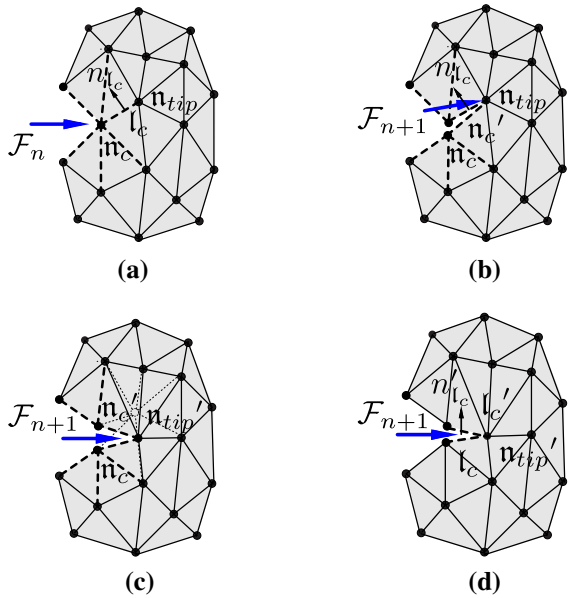

Fig. 4 Schematic view of the procedure of crack propagation. **a** Step I, **b** step II, **c** step III, **d** step IV

$$\mathfrak{l}_c := \arg\left\{ \inf_{\boldsymbol{X}_{\mathfrak{n}_{tip}} \in \partial \mathfrak{s}} \left(\left| \mathcal{F}_{n+1} \cdot \boldsymbol{n}'_{\mathfrak{l}} \right| \right) \right\} = \arg\left\{ \inf_{\boldsymbol{X}_{\mathfrak{n}_{tip}} \in \mathcal{B}} \left(\vartheta_{\mathfrak{n}_{tip}} \right) \right\}. \tag{36}$$

Here, $\mathfrak{s}$ represents the surface of the triangle elements connected to the crack tip node. The function $\vartheta_{\mathfrak{n}_{tip}}$ vanishes through the corrected crack growth direction. Repositioning of the new crack tip and the structure update have to be done and the above mentioned inner product has to be calculated until the equality $\vartheta_{\mathfrak{n}_{tip}} \rightarrow 0$ is achieved. This can be accomplished by reorienting the position of the new crack tip node $\boldsymbol{X}_{\mathfrak{n}_{tip}}$ from the reference position to the new position by using the NEWTON-RAPHSON method. This condition is satisfied after some iterations as shown in Fig. 4. The NEWTON-RAPHSON method may be obtained by the solution of the equation

$$\vartheta^{next}_{\mathfrak{n}_{tip}} = \vartheta^{prev}_{\mathfrak{n}_{tip}} + \partial_{\boldsymbol{X}_{\mathfrak{n}_{tip}}} \vartheta_{\mathfrak{n}_{tip}} \Delta \boldsymbol{X}. \tag{37}$$

Here, $\Delta \boldsymbol{X}$ is the unknown vector and it describes how much the position of the crack tip moves in order to obtain equilibrium of the equation. $\partial_{\boldsymbol{X}_{\mathfrak{n}_{tip}}} \vartheta_{\mathfrak{n}_{tip}}$ is the numerical tangent of the equation, which is obtained by an additional solution with a very small incremental change in the position of the node. It is used such that it is 100 times smaller than the size of the critical line element in the numerical studies. After the new position is found, the solution procedure continues with the next time step of the solution. It is important to note that this iterative method may fail in the case that Eq. (37) oscillates around the local maximum or minimum without converging to a root, but converging to the local maximum or minimum. Therefore, additional effort might be necessary for more complex problems.

The duplication of nodes separates connected elements in a single time step. This sudden release creates spurious waves which are emitted at the duplicated nodes and propagate as a high frequency oscillation into the structure. Fortunately, these spurious waves are eliminated by introducing additional forces at the duplicated nodes which work as a damping in the frozen time step. Detailed information on the specification and implementation of these "regularization forces" used in this contribution is discussed in Özenç (2016).

2.3.3 Crack propagation velocity

One of the advantages of a smeared crack representation is that no tracking of the discontinuities, which have to be retained in a discrete crack framework, is needed. Nevertheless, when evaluating the speed of the propagation of a crack, additional post-processing effort is necessary. The first stumbling block may be the definition of the crack tip itself. In Borden (2012), BORDEN proposes to find the crack tip at an isocurve with a certain defined phase-field value and calculates the propagation velocity explicitly. HOFACKER uses $\dot{\Gamma}$ in Hofacker and Miehe (2013), which is the rate of the crack surface Γ that is obtained by domain integration, and avoids the explicit definition of the crack tip. In the following, these two approaches are discussed and a detailed description of the algorithms implemented is given.

Evaluation of local phase-field values The calculation of an isocurve is a numerically expensive procedure itself, but it does not provide the position of the crack tip. Rather, the isocurve represents a line on which the crack tip resides. In order to define the position of the crack tip thoroughly, the current mean direction of crack propagation has to be specified. While this is trivial for the crack shown in Fig. 5, it becomes more complex for kinking or branching cracks and seems to be very challenging when applied to three-dimensional computations.

Furthermore, the specific phase-field value for the isocurve is in question. BORDEN proposes a value of $p = 0.75$, although, the theory states the crack discontinuity is represented by a phase-field value of $p = 1.00$. Figure 6 shows the phase-field of the branching crack and the correspondent isocurves for $p = 0.75/0.85/0.99$. Note that even though the rep-

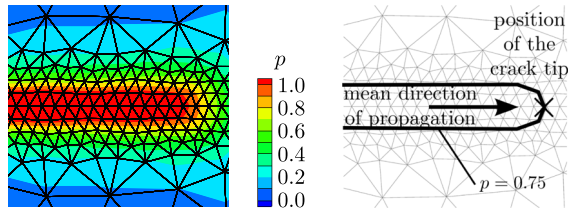

Fig. 5 Crack tip definition by an isocurve. **a** Phase-field distribution, **b** crack tip at isocurve $p = 0.75$

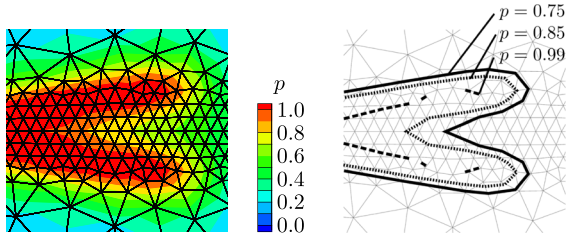

Fig. 6 Isocurve on different phase-field values. **a** Phase-field distribution, **b** isocurves at $p = 0.75/0.85/0.99$

resented crack is continuous, no continuous isocurve for $p \geq 0.98$ is present. While the computation of the isocurve is numerically expensive and the isocurve does not define the position of the crack tip without further work, a likewise procedure that only processes nodal values to find an approximate position of the crack tip is available. The procedure implemented is summarized subsequently. It is restricted to two-dimensional setups and a crack that propagates in positive x-direction. At first, the coordinates $x(t_0)$ and $y(t_0)$ of the initial crack tip at time $t_0 = 0\,\mathrm{s}$ have to be defined. Also, the limiting phase-field value p_{lim} has to be choosen. Every node with a phase-field value exceeding that limit is regarded to be a part of the crack's path. For every time t_n computed, the set of nodes with a phase-field value exceeding p_{lim} is found. The node out of this set with the largest coordinate in x-direction is defined to be the crack tip at time t_n. If the position differs from the one of the previous time, the crack is assumed to propagate and the new coordinates $x(t_n)$, $y(t_n)$ and the time of propagation t_n are stored. Here, n is an integer that starts at zero and increases by one every time the crack is assumed to propagate. As soon as all computed times are evaluated, the velocity of propagation $v_{cn}(t_n)$ from time t_{n-1} to t_n is calculated as

$$v_{cn}(t_n) = \frac{\sqrt{\Delta x^2 + \Delta y^2}}{\Delta t}, \tag{38}$$

with $\Delta x = x(t_n) - x(t_{n-1})$, $\Delta y = y(t_n) - y(t_{n-1})$ and $\Delta t = t_n - t_{n-1}$, for every time t_n the crack propagates.

Evaluation of volume integral The sharp crack surface Γ is approximated in the phase-field framework with the regularized crack surface Γ_l by

$$\Gamma \approx \Gamma_l = \frac{1}{2l} \int_\Omega p^2 + l^2 \, |\nabla p|^2 \, dV. \tag{39}$$

The surface of the crack Γ in a two-dimensional setting is equivalent to the length of the crack

$$l_c(t_n) = \frac{1}{2l} \int_\Omega p(t_n)^2 + l^2 \, |\nabla p(t_n)|^2 \, dV. \tag{40}$$

Assuming a constant velocity within a time step $\Delta t = t_n - t_{n-1}$, the velocity of crack propagation $v_{cv}(t_n)$ can be written as

$$v_{cv}(t_n) = \frac{l_c(t_n) - l_c(t_{n-1})}{t_n - t_{n-1}}. \tag{41}$$

While Eq. (41) contains the information on the crack surface Γ of the entire body Ω, it is only valid as long as a single crack is present. As soon as crack branching occurs or an additional crack develops, Eq. (41) represents the rate of the entire crack surface in the body. If the benefit of not needing to track discontinuities discretely is omitted, and particular crack tips are identified, the local evaluation of Eq. (39) around a crack tip yields more particular information about the evolution of a specific branch. Nevertheless, such a procedure is numerically expensive and complicated to implement in cases, where the phase-field of independent cracks influence each other.

In the material force approach, the crack tip is easily identified by the evaluation of the material force. The evaluation of the change of the position of the crack tip with Eq. (38) yields the correspondent crack propagation velocity in a straight forward manner.

3 Numerical examples

3.1 Interaction of waves and cracks

The first example investigates general principles of the propagation of stress waves and of the interaction of stress waves with a crack. The propagation of a longitudinal wave and its interaction with an initial crack is simulated. The geometry with dimensions $L = 100\,\mathrm{mm}$ and $H = 1\,\mathrm{mm}$ and the initial crack Γ are shown in Fig. 7. The crack surface is perpendicular to the wave propagation direction. Material parameters are $\lambda = 8.89\,\mathrm{GPa}$, $\mu = 13.33\,\mathrm{GPa}$ and $\rho = 2450\,\mathrm{kg/m^3}$. At its left edge, the specimen is subjected to a time dependent stress boundary condition $\sigma(t)$ that is sinusoidal with peak pressure $\hat{\sigma} = 1\,\mathrm{MPa}$ and duration $D = 3.2\,\mu\mathrm{s}$.

At first, the anticipated course of this numerical experiment is schematically illustrated in Fig. 8. The

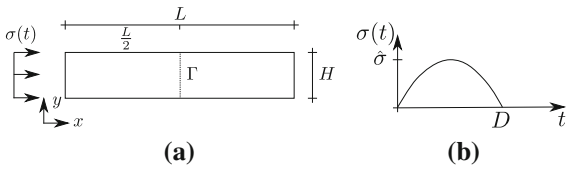

Fig. 7 Setup of stress wave traveling through a crack. **a** Geometry, **b** stress boundary

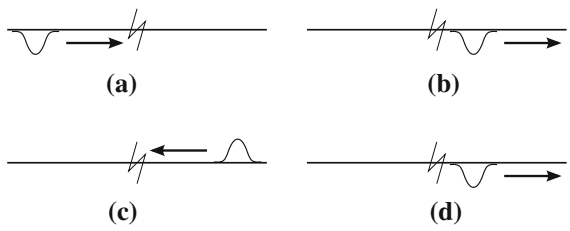

Fig. 8 Schematic view on the expected interaction of wave and crack. **a** Free propagation, **b** contact push through, **c** free edge reflection, **d** crack reflection

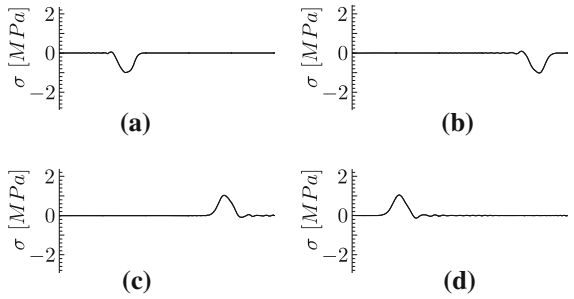

Fig. 9 Wave propagation in an uncracked specimen. **a** $t = 10\,\mu s$, **b** $t = 25\,\mu s$, **c** $t = 35\,\mu s$, **d** $t = 50\,\mu s$

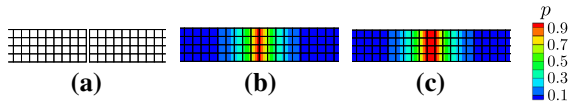

Fig. 10 Discrete and smeared approximation of the initial crack. **a** Discrete edge, **b** *one row* phase-field crack, **c** *two row* phase-field crack

horizontal direction of the Figures represent the length of the specimen in x-direction with the crack in the middle. The vertical direction represents the magnitude of the longitudinal stresses in the specimen, where tensile stresses are shown above the specimen and compressive stresses are shown below the specimen. Figure 8a shows a stress wave traveling from left to right towards the crack. Since this wave is compressive, it passes the crack by means of contact of the crack faces and proceeds towards the free edge, see Fig. 8b. At the free edge, the wave is reflected and propagates from right to left as a tensile wave as shown in Fig. 8c. For the tensile wave, the crack acts as a free edge. Thus, the wave is reflected at the crack and propagates from left to right as a compressive wave again as it is presented in Fig. 8d.

The next step is the simulation of the specimen without a crack with the NEWMARK time integration. The simulation results are shown, in a similar manner to the one above, in Fig. 9 that also contains the explicit value of the stresses. The simulation provides the means to check the general plausibility of the solution and to point out the characteristics of the wave propagation in a linear elastic material. According to Meyers (1994), a longitudinal wave propagates at the velocity $v_{\text{long}} = \sqrt{\frac{\lambda+2\mu}{\rho}} \approx 3810\,\text{m/s}$. Thus, it travels the entire specimen in $\approx 26\,\mu s$ which is in good agreement with the results depicted in Fig. 9b. Furthermore, the reflection of a fully evolved compressive stress wave on a free edge results in a tensile stress wave that travels in the opposite direction. This is also obtained in the simulation, see Fig. 9c. It is also worth to note the evolution of secondary waves following the primary wave and their growth in magnitude, which is a typical feature of wave propagation in a medium with a considerable POISSON's ratio.

The next simulation models the surfaces of the initial crack as a discrete edge in the mesh. Despite the material force is not used explicitly in this simulation, the realization of a crack by discrete edges in the mesh belongs to this approach. Two patches of height 1 mm and length 50 mm are discretized by 200×4 square elements each. A gap of length 0.1 nm separates the two patches as shown in the non-scale Fig. 10a. In order to model the transmission of compressive waves, contact nodes are introduced at the position of the crack's surfaces and a penalty method prevents the interpenetration of the crack surfaces. The result of the simulation is shown in Fig. 11. To model the expected behavior, an additional effort is necessary when defining the initial gap size as well as the contact stiffness. The initial gap needs to be small enough to enable contact from the beginning. The contact stiffness determines the amount of the compressive wave transmitted via the crack.

The modeling of initial cracks within the phase-field framework is described in Borden et al. (2012). All initial nodal phase-field values are set according to an analytically calculated phase-field pattern. The

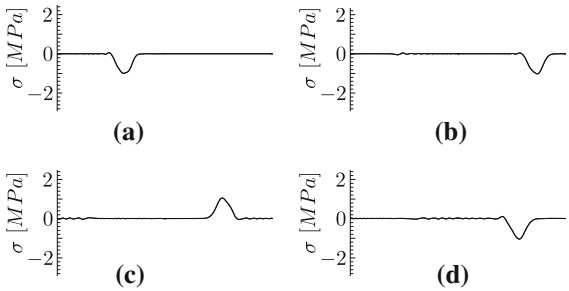

Fig. 11 Stress wave traveling through a discrete crack. **a** $t = 10\,\mu s$, **b** $t = 25\,\mu s$, **c** $t = 35\,\mu s$, **d** $t = 50\,\mu s$

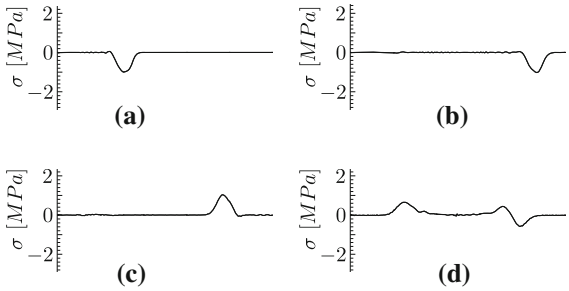

Fig. 12 Stress wave traveling through a *one row* phase-field crack. **a** $t = 10\,\mu s$, **b** $t = 25\,\mu s$, **c** $t = 35\,\mu s$, **d** $t = 50\,\mu s$

same result is achieved, when all nodes along the initial crack have boundary conditions $p = 1$ and no further mechanical loading is present, see e.g. Miehe et al. (2010a). The first attempt to model an initial phase-field crack uses the second method, i.e. imposes boundary conditions $p = 1$ to the nodes that coincide with the crack's location. The computed phase-field is shown in Fig. 10b. The transient simulation employs the standard implicit NEWMARK time integration and obtains the results shown in Fig. 12. The compressive wave passes the phase-field crack nearly unaffected, see Fig. 12b. After reflection at the free edge, the tensile wave approaches the phase-field crack as illustrated in Fig. 12c. Instead of the expected full reflection, like in the discrete model, a considerable amount of the wave passes the crack and only a portion of the initial wave is reflected, see Fig. 12d.

The reason of the problem of partial reflection at the phase-field crack is the degradation of the element stiffness on the element level. Each element contributes to the global stiffness K by evaluation of Eq. (9) at the GAUSS-points. The amount of degradation is specified by Eq. (8), i.e. the state of full degradation is reached only for $p = 1$. The computed initial phase-field is

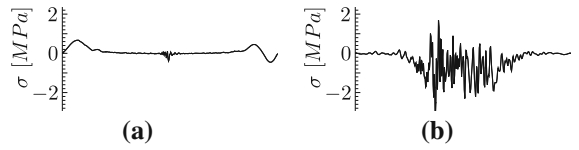

Fig. 13 Continued simulation of stress wave propagation for *one row* phase-field crack. **a** $t = 55\,\mu s$, **b** $t = 70\,\mu s$

equal to one at the nodes along the path of the initial crack and diminishes quickly inside the adjacent elements, see Fig. 10b. Therefore, the evaluation of Eq. (8) yields the fully degraded state for no GAUSS-point contribution at all. To force one element's stiffness contribution to be fully degraded, all nodes of this element must have $p = 1$. In consequence, initial cracks in dynamic phase-field computations have to be represented by a continuous sequence of elements along the crack path all having boundary condition $p = 1$ for each of their nodes. In this example this is achieved by imposing boundary conditions $p = 1$ to two adjoined rows of nodes in the vicinity of the crack's location. The computed phase-field is presented in Fig. 10c. In the following, this kind of continuous sequence of fully degraded elements is called "dynamic phase-field crack". However, the study shows another problem arising from phase-field cracks in combination with the standard NEWMARK time integration method. With the (partial) reflection of the tensile stress wave at the phase-field crack, a high frequency response is triggered. Its origin may already be suspected in Fig. 12d. The high frequency response reaches a considerable magnitude at $t = 55\,\mu s$, as shown in Fig. 13a, and the spurious stress waves dominate the solution at $t = 70\,\mu s$, see Fig. 13b.

The reason of the high frequency oscillation is directly related to the phase-field in combination with dynamic problems. The rule of thumb for an approximate time step necessary to simulate proper wave propagation is given by

$$\Delta t = h_{\min} \cdot \sqrt{\frac{\rho}{E}}, \tag{42}$$

with the minimum element size $h_{\min}$ in the structure. As the elastic modulus E is degraded in the vicinity of the crack, the time step size should grow locally. Due to the total degradation of the element stiffness in the vicinity of the crack, standard substepping methods are not suitable. Alternatively, the purely numerically induced high frequency response can be damped out

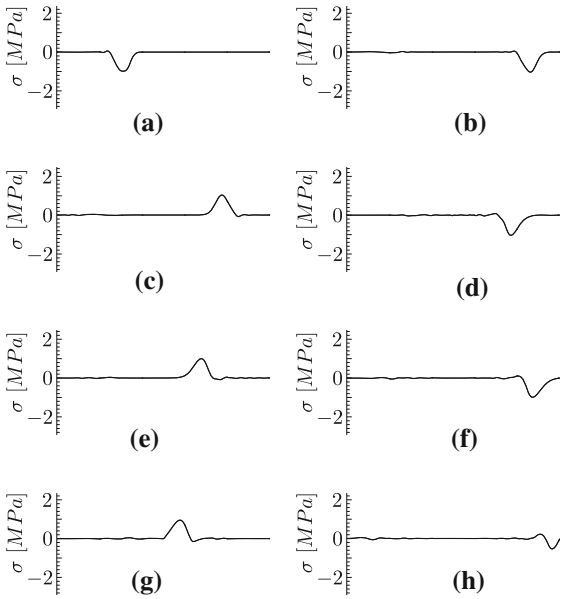

Fig. 14 Stress wave traveling through two row phase-field crack with HHT time integration. **a** $t = 10\,\mu s$, **b** $t = 25\,\mu s$, **c** $t = 35\,\mu s$, **d** $t = 50\,\mu s$, **e** $t = 65\,\mu s$, **f** $t = 80\,\mu s$, **g** $t = 95\,\mu s$, **h** $t = 110\,\mu s$

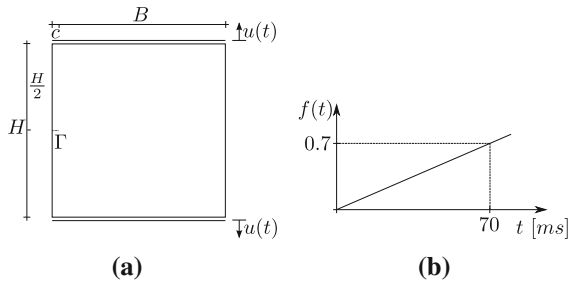

Fig. 15 Setup of FINEBERG's experimental crack propagation study. **a** Geometry, **b** time dependent loading

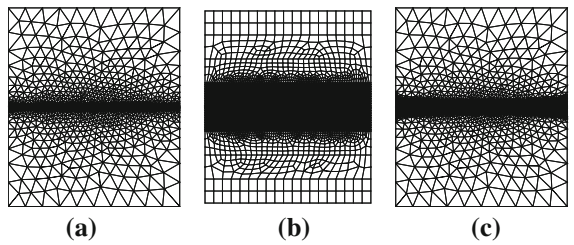

Fig. 16 Triangular element meshing. **a** Coarse mesh, **b** medium mesh, **c** fine mesh

by applying global damping, e.g. RAYLEIGH damping, but this also affects lower frequencies and changes the entire simulation. Instead, the HHT time integration method, mentioned in Sect. 2.3.1, is applied. The results of the phase-field crack wave interaction with an initial dynamic phase-field crack and application of the HHT time integration method are depicted in Fig. 14.

Thus, the introduction of an initial "dynamic phase-field crack" and the application of the HHT time integration method allow to simulate all the features of this experiment.

3.2 Crack tip velocity

In the second example, a thin PMMA specimen with width $B = 380\,\text{mm}$, height $H = 440\,\text{mm}$ and an initial crack Γ of length $c = 4\,\text{mm}$, as shown in Fig. 15a, is studied and the results are compared to the experimental ones in Sharon et al. (1996). Material parameters are $\lambda = 2.8\,\text{GPa}$, $\mu = 1.2\,\text{GPa}$ and $\rho = 1190\,\text{kg/m}^3$. In the experimental study, the upper and lower edge of the specimen are clamped. The clamps move away from each other in small displacement increments. Between each load increment, the displacement is kept constant for a period of 10–20 s in order to have a static stress distribution at the crack tip. At a displacement strongly affected by the shape of the initial notch, the onset of crack propagation is observed and the velocity of the crack propagation is measured. The crack propagates straight in horizontal direction to the vertical edge without branching macroscopically. The microscopic review of the crack surface in Fineberg et al. (1992) shows a set of three typical crack stages, named by *mirror*, *mist* and *hackle*. As the crack propagates at the beginning, the smooth *mirror* region is created with microscopical planar crack surfaces. With increased propagation velocity, the crack surfaces become rougher in the *mist* region. Finally, in the *hackle* region, micro branches evolve and stop after a short period of growth. While the macroscopically observed crack path is straight and linear, the crack surface created by micro branches increases up to over 5 times the surface formed by a single crack.

The structure is discretized by triangular elements with refinement along the expected crack path, see Fig. 16. The meshes for the phase-field simulation consist of 6230 (Fig. 16a) and 18,412 (Fig. 16c) elements with minimum element sizes $h_{min} = 0.89\,\text{mm}$ and $h_{min} = 0.7\,\text{mm}$, respectively. A constant length scale of $l = 2.0\,\text{mm}$ is used for both meshes in order to make the calculations comparable. For the material force sim-

ulation, a mesh with 8881 (Fig. 16b) elements is used. In order to keep the number of total elements as small as possible, only the expected path of the crack is refined with triangular elements. The initial crack is modeled by a discrete gap between the elements adjacent to the crack's surface for both approaches. The experimental loading with long periods of constant loading is not suitable for a fully transient calculation. Therefore, the prescribed edge loading $u(t) = \hat{u} \cdot f(t)$, with $\hat{u} = 3.5\,\text{mm}$ and $f(t)$ according to Fig. 15b, is used and the calculation is divided into two stages. A quasi static simulation computes the stress distribution just before the onset of crack propagation and a subsequent transient calculation simulates the process of crack propagation itself with all related dynamic effects. The quasi static calculation is in fact a transient solution with big time steps. As the time steps are decreased in the calculation, transient effects gain importance till a fully transient calculation is performed at a time step according to Eq. 42, i.e. time steps $\Delta t = 0.15\,\mu\text{s}$ and $\Delta t = 0.19\,\mu\text{s}$ for the coarse and the fine mesh, respectively.

The simulation by the material force approach is carried out by the standard implicit NEWMARK time integration and starts with a time increment of $\Delta t = 1\,\text{s}$. After the computation of 3 static steps, the criterion for crack propagation is satisfied and the transient calculation continues with a time step of $\Delta t = 0.1\,\mu\text{s}$. The results show the propagation of a single straight crack because no branching criterion is defined. Nevertheless, the energy, which is required to initiate crack propagation, has to account for the additional dissipation in the micro-cracks formed near the crack tip at high crack propagation velocities. Therefore, a dynamic fracture criterion is introduced as the function of the crack velocity in Eq. 27 with parameters $v_{lim} = 701\,\text{m/s}$ and $\alpha = 0.25$. The proposed function and its fit to the experimental data published in Sharon et al. (1996) are represented in Fig. 17 for PMMA type of material.

The simulations by the phase-field approach employ the HHT time integration and start with a time increment of $\Delta t = 1\,\text{s}$. The time step is divided by ten each time the phase-field evolves to a nodal value of $p \geq 0.6$. Arriving at a time step of $\Delta t = 0.1\,\mu\text{s}$, the time step size stays constant and 2000 steps are computed. The initial quasi static calculation is performed till $t = 2.23575\,\text{s}$ and $t = 2.132348\,\text{s}$ for the coarse and the fine meshing, respectively.

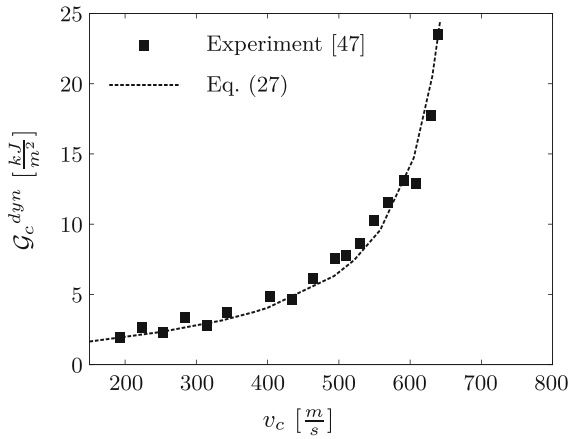

Fig. 17 Dynamic fracture energy $\mathcal{G}_c{}^{dyn}$ versus velocity of crack propagation v_c

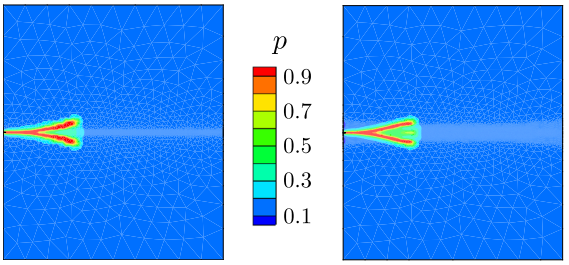

Fig. 18 Final path of the phase-field crack. **a** Coarse mesh, **b** fine mesh

The computed final phase-field after 2000 transient steps is shown in Fig. 18. The phase-field crack approximation simulates a single branch crack propagation until a crack length of ≈54 mm in the coarse mesh. Then, the crack branches into 2 macro branches enclosing an angle of 25°. The branching is already indicated by a widening of the phase-field that starts after 689 μs of transient simulation. The fine mesh shows straight crack propagation till ≈45 mm and then branching enclosing an angle of 25° again. Here, the widening starts after 588 μs of transient simulation. The branching indicates, that the amount of energy available for crack propagation exceeds the amount of energy necessary for the propagation of a single branch. The additional amount of energy is dissipated by the widening at first and finally by the formation of an additional crack branch. In contrast to the material force approach, the phase-field approach employs a constant fracture toughness $\mathcal{G}_c$, that is independent of the crack propagation velocity. Therefore, the material force approach

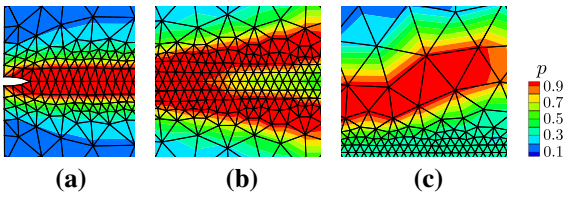

Fig. 19 Close look to the final phase-field distribution in the coarse mesh. **a** Initiation point, **b** macro-branch, **c** invalid length scale results

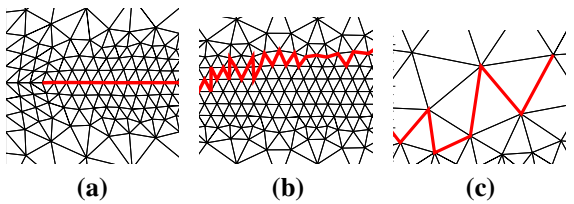

Fig. 20 Path of the phase-field crack evaluated by the nodal method. **a** Initiation point, **b** macro-branch, **c** invalid length scale results

simulates a straight propagation while the branching is obtained with the phase-field approach.

Another problem arises from the general properties of dynamic phase-field cracks in combination with the computation of the crack propagation velocity based on nodal phase-field values as outlined in Sect. 2.3.3. It is particularly significant for triangular element meshes. Based on the set of nodes that are supposed to be the crack tip, the path of the crack should be represented by the line connecting these nodes. Unfortunately, only for special cases this path is congruent to the crack path assumed intuitively. While the crack is propagating straight, the method shows a good approximation of the crack path, see Figs. 19a and 20a. The problem occurs as soon as the phase-field crack widens, branches or propagates in coarsly meshed regions, see Figs. 19b, c. Instead of an intuitively assumed smooth crack path, there is a zig-zag-pattern, as seen in Figs. 20b, c. This leads to an increase of the total length of the crack by a considerable amount. In consequence, the calculated velocity of crack propagation is overestimated. The results can be improved by the modification of Eq. (38) into

$$v_{cn}(t_n) = \frac{\sqrt{\Delta x_{10}{}^2 + \Delta y_{10}{}^2}}{\Delta t_{10}} \tag{43}$$

with $\Delta x_{10} = x(t_n) - x(t_{n-10})$, $\Delta y_{10} = y(t_n) - y(t_{n-10})$ and $\Delta t_{10} = t_n - t_{n-10}$. Instead of the path to the next node in the set of crack tip nodes, the 10th next node in the set is used. This assumption smooths the evaluated crack path and gives a more realistic estimation of the actual speed of crack propagation. Still, this is not the optimal way to calculate the real velocity of crack propagation. Rather, it represents an upper limit which the exact velocity of crack propagation does not exceed.

The domain integration approach to the calculation of the crack velocity, based on the volume integral of Eq. (39), suffers from two facts. First of all, the phase-field crack evolves as a dynamic phase-field crack, i.e. a continuous sequence of fully degraded elements along the crack's path is obtained and the phase-field widens, see Fig. 19. In consequence, the approximated crack surface in the specimen is overestimated as well as the velocity of crack propagation. In addition, the length scale is adjusted to the small size of elements in the refined regions. Whenever the crack propagates in coarsly meshed parts of the structure, the overestimation of the crack surface increases even more. Furthermore, as already mentioned, Γ_l contains the whole crack surface inside the body. The corresponding velocity computation v_{cv} is assigning this entire crack surface to the length of a single crack. For example, as soon as the crack branches, v_{cv} is giving at least two times the value of the actual velocity of crack propagation.

The calculated and measured crack propagation velocities are plotted with respect to time in Figs. 21 and 22 for the coarse and the fine mesh, respectively. The results of the material force and the phase-field approach are abbreviated by "MF" and "PF", respectively. The phase-field simulations are evaluated with the nodal method by Eq. (38), its modification by Eq. (43) and the energetic method by Eq. (41). Here,

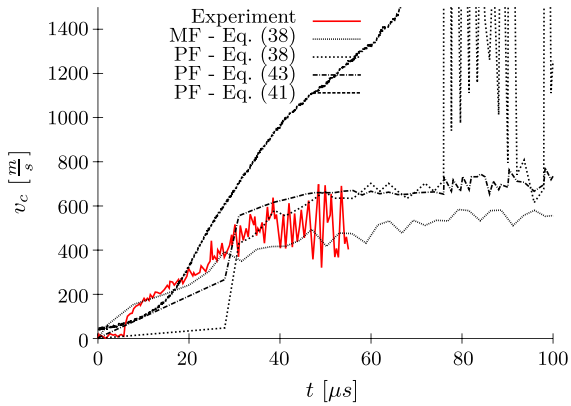

Fig. 21 Velocity of crack propagation in the coarse mesh

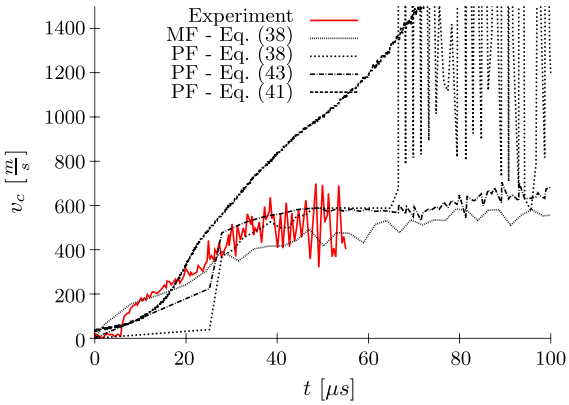

Fig. 22 Velocity of crack propagation in the fine mesh

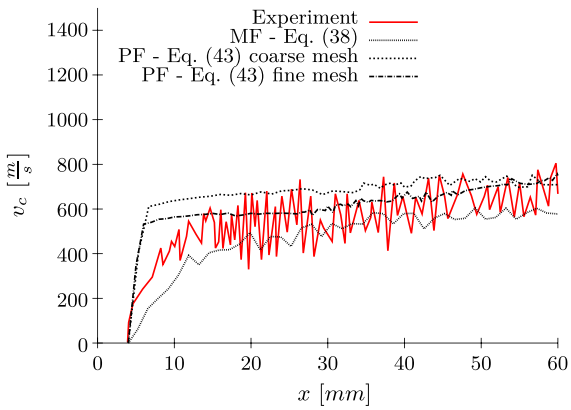

Fig. 23 Velocity of crack propagation with respect to the crack length

the nodal methods incorporate the limiting phase field value $p_{\text{lim}} = 0.95$. The results are shown in the way that time $t = 0\,\text{s}$ represents the onset of the propagation of the crack, which is unique and not identical in all the simulations. In the material force calculation, the propagation starts in the first transient step, while in phase-field simulations no explicit moment can be identified. While the domain integration method indicates a growth of the crack surface for the very first step of the transient calculation, the nodal method shows that the crack propagation starts ≈25 µs later and the energetic method only shows the growth of crack surface due to the widening. Nevertheless, $t = 0\,\text{s}$ corresponds to the moment when the domain integration method indicates the first growth of the crack surface in the transient part of the simulation. First of all, the material force results show very good agreement compared to the measurement due to the calibration of the dynamic fracture criterion with the experimental data. Also, as discussed above, the calculation of the velocity of crack propagation by the evaluation of nodal phase-field values results in unrealistic values as soon as no straight phase-field crack propagation is present any more, i.e. at ≈75 µs and ≈65 µs after the onset of crack propagation in the coarse mesh and the fine mesh, respectively. Nevertheless, the results of the nodal evaluation, smoothed by the application of Eq. (43), are an upper limiter for the real velocity of crack propagation. The energetic method overestimates the crack propagation velocity and is useless for the comparison of the propagation velocities. However, it presents additional information on the formation of the phase-field crack, e.g. the numerical crack surface continuously grows in the transient part of the simulation. Furthermore, compared to experimental results, the numerical crack surface of the phase-field simulations is up to three times higher than expected.

Another representation of the results is shown in Fig. 23 by the plot of the crack propagation velocity with respect to the crack length. Here, the experimental results are compared to the material force results and the results of the smoothed nodal approach for the phase-field simulations for the coarse mesh and the fine mesh. The material force approach shows the acceleration of the crack propagation until the propagation velocity of 400 m/s. Then, similar to the experimental results, the acceleration decreases and the velocity does not exceed the value of 500 m/s which is a good approximation for the lower limiter of the experimentally measured crack propagation speed. The acceleration period in the phase-field simulation is shorter but the acceleration is faster than the experimental one. Furthermore, after acceleration, the phase-field crack propagates at a velocity around 600 m/s which is a good approximation for the upper limiter of the experimentally measured crack propagation speed.

3.3 Dynamic crack branching

In this numerical study, the macro crack branching phenomenon is investigated by both approaches introduced. The specimen, with heigth $H = 40\,\text{mm}$, width $B = 100\,\text{mm}$ and an initial crack Γ with length $\frac{B}{2} = 50\,\text{mm}$, is depicted in Fig. 24a.

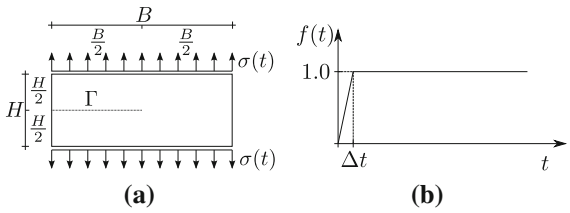

Fig. 24 Dynamically loaded sample for crack branching. **a** Geometry, **b** time dependent loading

The material is characterized by an elastic modulus $E = 32\,\text{GPa}$, a POISSON's ratio $\nu = 0.2$ and a density $\rho = 2450\,\text{kg/m}^3$. The fracture constant for the phase-field model is $\mathcal{G}_c = 3\,\text{J/m}^2$ and, for the material force approach, the dynamic fracture criterion is used with $v_{lim} = 891\,\text{m/s}$ and $\alpha = 2.5$. The specimen is subjected to a time dependent stress boundary $\sigma(t) = \hat{\sigma} \cdot f(t)$ with $\hat{\sigma} = 1\,\text{MPa}$ and $f(t)$ as shown in Fig. 24b. The finite element mesh consists of 400×160 (coarse), 800×320 (medium) and 1600×640 (fine) quadrilateral elements with a constant element size of $h = 250\,\mu\text{m}$, $h = 125\,\mu\text{m}$ and $h = 62.5\,\mu\text{m}$, respectively. Although this example is already simulated by BORDEN with the phase-field approach in Borden et al. (2012), two main differences in the presented simulation have to be distinguished. First, the initial crack is modelled discretely by separation of the elements. Then, in contrast to BORDEN's calculation, also the length scale is adapted to the element size to $l_{\text{coarse}} = 500\,\mu\text{m}$, $l_{\text{medium}} = 250\,\mu\text{m}$ and $l_{\text{fine}} = 125\,\mu\text{m}$. The computation is performed from $t = 0\,\mu\text{s}$ to $t = 80\,\mu\text{s}$ with constant time steps $\Delta t_{\text{coarse}} = 0.1\,\mu\text{s}$, $\Delta t_{\text{medium}} = 0.05\,\mu\text{s}$ and $\Delta t_{\text{fine}} = 0.025\,\mu\text{s}$.

The resultant paths of the crack are visualized in Fig. 25. The general crack paths are similar in all simulations and the branching angles are $\approx 60°$ for all 6 simulations. However, for the phase-field model, the smaller the length scale is, the later the branching occurs. This should not be confused with mesh sensitivity. As already shown in the study of BORDEN, equal results are obtained in the case of a constant length scale for all 3 meshes. Rather, in addition to fracture toughness, the length scale acts as a material parameter with significant impact onto the results in dynamic calculations, where the limiting case of $l \to 0$ may not be possible due to various reasons. The results of the material force approach are objective, making the position of the branching and the branching angles independent of the mesh size. The branching criterion in Eq. (28) incorporates $m = 4.54$ to meet the branching pattern of the phase-field calculation with a length scale of $l = 500\,\mu\text{m}$. Furthermore, a detailed review of the phase-field distribution at the initial crack tip, the position of the branching and the kinking are given in Fig. 26a, b, c, respectively. It is important to take note of the evolution of the crack path as a continuous sequence of fully degraded elements. Because of the symmetry of the example, there are actually two rows of fully degraded elements forming the straight part of the crack before branching which increases the computed crack surface even more. Figure 26d, e f show the results for the material force evaluation at the final iteration step before crack propagation.

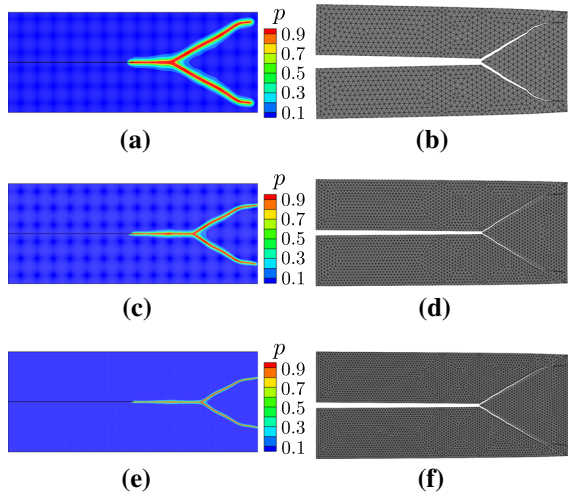

Fig. 25 Final path of the crack at $t = 80\,\mu\text{s}$. **a** PF coarse mesh, **b** MF coarse mesh, **c** PF medium mesh, **d** MF medium mesh, **e** PF fine mesh, **f** MF fine mesh

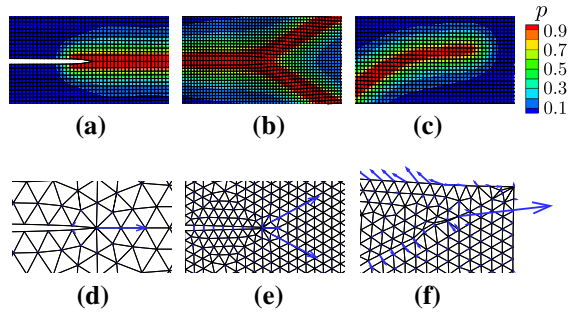

Fig. 26 Detailed view on the path of the crack in the coarse mesh simulations. **a** PF initial tip, **b** PF branch, **c** PF kink, **d** MF initial tip, **e** MF branch, **f** MF kink

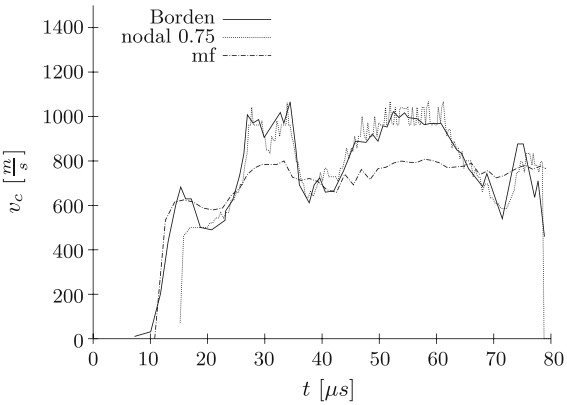

Fig. 27 Evaluation of the velocity of the crack propagation

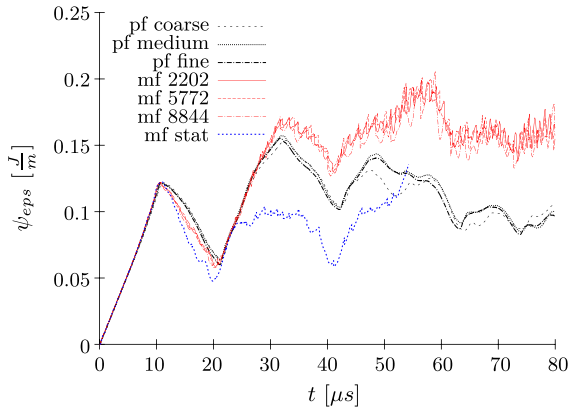

Fig. 28 Comparison of the strain energy of the entire structure

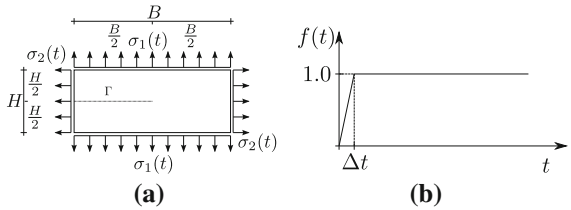

Fig. 29 Extension of the dynamic example of crack branching. **a** Geometry, **b** time dependent loading

Figure 27 shows the plot of crack propagation velocity versus time for the material force approach, the phase-field approach and the results published in Borden et al. (2012), which are also simulated with the phase-field formulation. For the first 20 µs, the velocity of crack propagation of BORDEN's study and the material force approach agree very well, while our phase-field crack model starts to propagate later. For the rest of the simulation, both phase-field approaches are in a good agreement. The material force approach shows slower crack propagation due to the dynamic fracture criterion which introduces an additional limiter to the crack propagation velocity.

Figure 28 depicts the strain energy stored in the structure with respect to time for the phase-field approach and the material force approach with the static and the dynamic fracture criterion. Although the crack already starts to propagate at $t = 10\,\mu s$, both material force simulations show the same amount of strain energy in the structure up to $t = 25\,\mu s$. After this time, the modified dynamic criterion for the material force has an effect. Due to an increased velocity of crack propagation, the energetic level necessary for further crack propagation increases and the crack propagates at a later time. Therefore, at the same solution time, more energy dissipates into the crack surface for the material force simulation with the static criterion resulting in less energy left over in the structure for the strain energy. With a constant fracture criterion, the material force approach simulates the total failure much earlier, because the energy is dissipated faster. The results of the phase-field simulations are in between the results for the static and the dynamic fracture criterion and are also shown in Fig. 28.

3.4 Dynamic crack branching study at biaxial tension specimen

This example is an extension of the previous example, where bi-axial loads are applied in order to influence the crack pattern (Fig. 29). The size of the specimen, material parameters and fracture criteria specifications remain the same as in the previous section. Only one meshing with 400 × 160 quadrilateral elements is used. Correspondently, the phase-field length scale is $l = 500\,\mu m$. The stress boundaries at the vertical and horizontal edge of the specimen, $\sigma_1(t)$ and $\sigma_2(t)$, respectively, are chosen to create tension stresses. They are defined by the time dependent loading function $\sigma_1(t) = \hat{\sigma} \cdot f(t)$ and $\sigma_2(t) = k \cdot \hat{\sigma} \cdot f(t)$, with $\hat{\sigma} = 1$ MPa and k the ratio of horizontal and vertical loading. A value of $k = 0$ corresponds to the results of the coarse mesh simulations in Sect. 3.3. Simulations are performed for $k = 0.5$, $k = 1.0$ and $k = 2.0$ with a constant time step of $\Delta t = 0.1\,\mu s$.

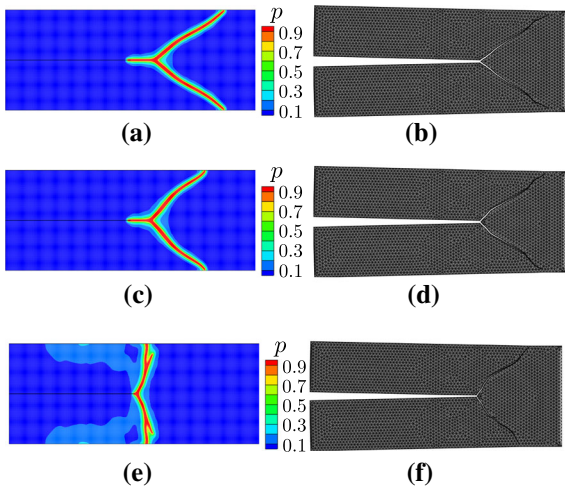

Fig. 30 Final path of the crack in phase-field and material force simulations. **a** $k = 0.5$ and $t = 73\,\mu s$, **b** $k = 0.5$ and $t = 80\,\mu s$, **c** $k = 1.0$ and $t = 65.5\,\mu s$, **d** $k = 1.0$ and $t = 80\,\mu s$, **e** $k = 2.0$ and $t = 33\,\mu s$, **f** $k = 2.0$ and $t = 80\,\mu s$

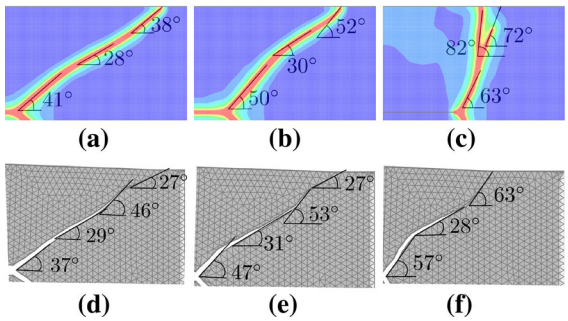

Fig. 31 Extraction of the angles for phase-field and material force simulations. **a** $k = 0.5$, **b** $k = 1.0$, **c** $k = 2.0$, **d** $k = 0.5$, **e** $k = 1.0$, **f** $k = 2.0$

The resultant crack paths are visualized in Fig. 30. A detailed review of the direction of propagation is presented in Fig. 31. In the following, the direction of propagation of the crack is described by the angle between the two branches, which are double to the values presented in Fig. 31 due to symmetry of the problem.

For the minor lateral load ($k = 0.5$), the straight crack bifurcates into two main branches enclosing an angle of 82° and 74° for phase-field and material force simulation, respectively. In the phase-field simulation, kinking of the crack is observed two times, but in contrast to the material force calculations, the change of the direction of propagation is smooth and continuous without any sharp edges. In the phase-field simulation, the initial angle is first reduced to 56° and then increases again to 76° before the crack reaches the horizontal edge of the specimen at $t = 73\,\mu s$. The material force calculation shows three times kinking. The initial angle of 74° decreases to 58°, jumps onto 92° and then decreases again to 54°. At the end of calculation, at $t = 80\,\mu s$, the crack does not touch the boundary of the specimen.

With the medium lateral load ($k = 1.0$), the initially enclosed angles are 100° and 94° for the simulation of the phase-field and the material forces, respectively. While material forces simulate the crack branching at exactly the same position as for $k = 0.0$ and $k = 0.5$, the length of the straight part of the phase-field crack calculated for $k = 1.0$ is shortened by 1.8 mm compared to the results for $k = 0.5$. Furthermore, the phase-field shows a constant reduction of the initial angle down to a value of 60°. Just before the crack reaches the outer boundary at $t = 65.5\,\mu s$, the angle increases to 104°. In the material force results, the angle changes 3 times before the end of calculation at $t = 80\,\mu s$. The crack does not reach the outer boundary of the specimen at this time. The angle starts with an initial value of 94°, decreases to 62°, increases to 106° and decreases again to 54°.

The major lateral load ($k = 2.0$) creates additional features in the phase-field crack pattern that are not observed for the material force simulations. After 1 mm of straight crack propagation, the phase-field crack bifurcates into branches enclosing an angle of 126°. This angle continuously increases to a value of 144° at $t = 25\,\mu s$ and, then, the branch starts to bifurcate again. The lower branch continues straight at 144° and stops at $t = 31\,\mu s$, while the upper branch turns up to 164° and reaches the outer boundary of the specimen at $t = 33\,\mu s$. Again, the lateral load shows minor effect on the position of the branching in the material force simulation. The axial stresses of the mode I loading direction primarily determine the position, where the material force is large enough to satisfy the branching criterion. As these stresses are the same for all the calculations, the position of branching is close in the simulations. After branching, the lateral load has an effect. The angle of branching is the result of a procedure to minimize the energy in the configuration after branching. Here, lateral stresses create mixed mode crack tip loading and influence the direction of propagation directly. For $k = 2.0$, the initial angle between the branches is 114°. This angle drops to 56° and jumps to 126° again.

The simulations show no direct agreement between the results of the phase-field and the material force approaches, but common tendencies are observed. Generally, the initial angle between the branches increases with an increased lateral load. Also, the initial angles are in the same range for phase-field and material force simulations. The only question remaining is whether the phase-field description represents the influence of lateral stresses correctly. On the one hand, from the energetic point of view, the additional contribution of the horizontal stress and strain to the available energy for dissipation is clear. In consequence, the level necessary for branching has to be reached earlier. On the other hand, the point of view in the material force method also sounds reasonable. If we visualize the initial crack as a zipper and the material force as the "opening force" for the zipper, it is never opened by a horizontal loading, i.e. T-stresses. Therefore, horizontal stresses have only a minor contribution to the "opening force" in this case. Nevertheless, the computations show that the direction of propagation after branching is affected by the horizontal loading.

The changes of the direction of propagation after branching are quite large and show totally different behavior for the phase-field and the material force simulations. At this point, it is worth to note that the vertical load induces a stress wave that travels to the crack tip in about $5\,\mu s$. Therefore, the simulation time of $80\,\mu s$ allows the wave to be reflected several times and to influence the tip more than once. Under consideration of the fact that with the different positions of branching, totally different structures with completely different potential for wave reflection and interaction are investigated, it is evident that the results are hardly comparable at this stage.

4 Conclusion

The first numerical study in this publication investigates two main features of the interaction between wave propagating in a continuum and a pre-existing crack. On the one hand, the transmission of compressive stress waves by the means of contact of the crack surfaces is found and, on the other hand, the reflection of tensile stress waves by means of wave reflection at a free edge of a continuum is obtained. The material force approach focuses on the crack evolution and realizes the crack by separated element edges. The simulation of the crack closure and the transmission of forces requires the introduction of contact, because the separated element edges have to interact with each other. Some effort has to be put into the definition and calibration of the contact method and its parameters to obtain a realistic result. The discrete approach gives good results with the standard implicit NEWMARK time integration method. The initial phase-field crack is realized by boundary conditions forming a continuous sequence of fully degraded elements along the crack path. While this is the only way to obtain realistic wave crack interaction results, it also results in an overestimated size of the numerical crack surface. Furthermore, it is necessary to apply numerical damping in order to suppress spurious oscillations.

The second numerical study presents the evaluation of the velocity of crack propagation and the comparison to an experimental result. The material force approach shows very good agreement with the experimentally measured values of the crack propagation velocity when the modified dynamic fracture criterion is adjusted to the experimental results. In case of the phase-field simulations, only the modification of one of the presented approaches to calculate the velocity of crack propagation is able to produce satisfying results. The domain integration method overestimates the created crack surface and results in unrealistic large values for the crack propagation speed but the nodal approach for the crack tip propagation velocity yields reasonable results with the smoothing modification. Nevertheless, the phase-field simulations suffer from the fact, that it is not possible to obtain the experimental crack pattern for the entire simulation.

Two possible solutions are available for this problem. The first solution may be a modification similar to the dynamic fracture criterion of the material force approach. Instead of constant fracture parameters, a rate dependent surface energy in agreement with the experimental results should be introduced. Another solution may simply be the refinement of the mesh in order to represent the governing processes on the microscale.

The third and fourth numerical study examine the ability of the applied methods to simulate the phenomenon of branching. The material force approach requires an additional criterion for branching. The phase-field approach implies the possibility for branching in its energetic origin and models branching without further implementations necessary. In phase-field

simulations, the results, especially the position of the branching, are sensitive to the size of the length scale and the lateral loading of the crack tip. In contrast, the material force simulations are objective and show only minor changes of the position of branching if lateral loads are present. Nevertheless, the angle encompassed by the branches are close for the material force and the phase-field approach.

This study shows, that discrete and smeared state of the art crack approximations are able to predict dynamic fracture reasonably, if the contributions of inertia are taken into account. Also, two topics of further research are identified. First of all, the relation between the energy dissipated by the crack propagation and the velocity of propagation of the crack has to be incorporated into the phase-field method. Secondly, the impact of lateral stresses on the phenomenon of branching has to be unraveled to obtain the correct results for crack propagation under multiaxial loading.

Acknowledgments The authors would like to acknowledge the financial support of "Deutsche Forschungsgemeinschaft" under grant KA 1163/19-1 and as well the technical support of the center for information services and high performance computing of the TU Dresden for providing access to the Bull HPC-Cluster. Moreover, we would like to thank ANSYS, Inc. for supporting Kaan Özenç.

References

Ambati M, Gerasimov T, Lorenzis LD (2015) A review on phase-field models of brittle fracture and a new fast hybrid formulation. Comput Mech 55:383–405

Amor H, Marigo JJ, Maurini C (2009) Regularized formulation of the variational brittle fracture with unilateral contact: numerical experiments. J Mech Phys Solids 57:1209–1229

Arakawa K, Takahashi K (1991) Relationship between fracture parameters and surface roughness of brittle polymers. Int J Fract 48:103–114

Bergkvist H (1974) Some experiments on crack motion and arrest in polymethylmethacrylate. Eng Fract Mech 6:621–626

Borden M (2012) Isogeometric analysis of phase-field model for dynamic brittle and ductile fracture. PhD thesis, The University of Texas at Austin

Borden MJ, Verhoosel CV, Scott MA, Hughes TJR, Landis CM (2012) A phase-field description of dynamic brittle fracture. Comput Methods Appl Mech Eng 217–220:77–95

Bourdin B (2007) The variational formulation of brittle fracture: numerical implementation and extensions. IUTAM Symp Discret Methods Evol Discontin 5:381–393

Bourdin B (2008) The variational approach to fracture. J Elast 91:5–148

Braides A (2002) Gamma-convergence for beginners. Oxford University Press, Oxford

Braun M (1997) Configurational forces induced by finite-element discretization. Proc Estonian Acad Sci Phys Math 35:379–386

Brouzoulis J, Larsson F, Runesson K (2010) Strategies for planar crack propagation based on the concept of material forces. Comput Mech 3:295–304

Dally J (1979) Dynamic photoelastic studies of fracture. Exp Mech 19:349–361

Fineberg J, Gross SP, Marder M, Swinney H (1992) Instability in the propagation of fast cracks. Am Phys Soc 45:5146–5154

Francfort GA, Marigo JJ (1998) Revisiting brittle fracture as an energy minimization problem. J Mech Phys Solids 46:1319–1342

Griffith AA (1921) The phenomena of rupture and flow in solids. Philos Trans R Soc London Ser A 221:163–198

Gürses E, Miehe C (2009) A computational framework of three-dimensional configurational-force-driven brittle crack propagation. Comput Methods Appl Mech Eng 198:1413–1428

Gurtin ME (2000) Configurational forces as basic concepts of continuum physics. Springer, New York

Hilber H, Hughes T, Taylor R (1977) Improved numerical dissipation for the time intergration algorithms in structural dynamics. Earthq Eng Struct Dyn 5:283–292

Hofacker M (2013) A thermodynamically consistent phase field approach to fracture. PhD. thesis, Universität Stuttgart

Hofacker M, Miehe C (2013) A phase field model of dynamic fracture: robust field updates for the analysis of complex crack patterns. Int J Numer Methods Eng 93:276–301

Hofacker M, Welschinger F, Miehe C (2009) A variational-based formulation of regularized brittle fracture. Proc Appl Math Mech 9:207–208

Karma A, Kessler DA, Levine H (2001) Phase-field model of mode III dynamic fracture. Phys Rev Lett 87(4):045501

Kienzler R, Herrmann G (2000) Mechanics in material space: with applications to defect and fracture mechanics. Springer, Berlin

Kobayashi AS, Mall S (1978) Dynamic fracture toughness of homalite-100. Exp Mech 18:11–18

Kobayashi AS, Wade BG, Bradley WB, Chiu ST (1972) Crack branching in homalite-100 sheets. Off Nav Res 13:1–29

Kuhn C, Müller R (2010) A continuum phase field model for fracture. Eng Fract Mech 77:3625–3634

Kuhn C, Müller R (2011) A new finite element technique for a phase field model of brittle fracture. J Theor Appl Mech 49:1115–1133

Maugin GA (2010) Configurational forces: thermomechanics, physics, mathematics, and numerics. CRC Press, Boca Raton

Maugin GA, Trimarco C (1992) Pseudomomentum and material forces in nonlinear elasticity: variational formulations and application to brittle fracture. Acta Mech 94:1–28

Menzel A, Denzer R, Steinmann P (2004) On the comparison of two approaches to compute material forces for inelastic materials. Application to single-slip crystal-plasticity. Comput Meth Appl Mech Eng 193:5411–5428

Meyers MA (1994) Dynamic behavior of materials. Wiley, New York

Miehe C, Gürses E (2007) A robust algorithm for configurational-force-driven brittle crack propagation with r-adaptive mesh alignment. Int J Numer Methods Eng 72:127–155

Miehe C, Hofacker M, Welschinger F (2010) A phase field model for rate-independent crack propagation: robust algorithmic implementation based on operator splits. Comput Methods Appl Mech Eng 199:2765–2778

Miehe C, Welschinger F, Hofacker M (2010) Thermodynamically consistent phase-field models of fracture: variational principles and multi-field fe implementations. Int J Numer Methods Eng 83:1273–1311

Müller R, Maugin GA (2002) On material forces and finite element discretizations. Comput Mech 29:52–60

Näser B, Kaliske M, Dal H, Netzker C (2009) Fracture mechanical behaviour of visco-elastic materials: application to the so-called dwell-effect. Z Angew Math Mech 89:677–686

Ortiz M, Pandolfi A (1999) Finite-deformation irreversible cohesive elements for three-dimensional crack-propagation analysis. Int J Numer Methods Eng 44:1267–1282

Özenç K, Kaliske M (2014) An implicit adaptive node-splitting algorithm to assess the failure mechanism of inelastic elastomeric continua. Int J Numer Meth Eng 100:669–688

Özenç K, Kaliske M, Lin G, Bashyam G (2014) Evaluation of energy contributions in elasto-plastic fracture: a review of the configurational force approach. Eng Fract Mech 115:137–153

Özenç K, Chinaryan G, Kaliske M (2016) A configurational force approach to model the branching phenomenon in dynamic brittle fracture. Eng Fract Mech 157:26–42

Pandolfi A, Ortiz M (2002) An efficient adaptive procedure for three-dimensional fragmentation simulations. Eng Comput 18:148–159

Ramulu M, Kobayashi AS (1985) Mechanics of crack curving and branching—a dynamic fracture analysis. Int J Fract 27:187–201

Ravi-Chandar K, Knauss W (1984) An experimental investigation into dynamic fracture: III. On steady-state crack propagation and branching. Int J Fract 26:141–154

Rice JR (1968) Mathematical analysis in the mechanics of fracture, vol 2. Academic Press, New York

Schlüter A, Willenbücher A, Kuhn C, Müller R (2014) Phase field approximation of dynamic brittle fracture. Comput Mech 54:1141–1161

Schütte H (2009) Curved crack-propagation based on configurational forces. Comput Mater Sci 46:642–646

Sharon E, Gross SP, Fineberg J (1996) Energy dissipation in dynamic fracture. Phys Rev Lett 76:2117–2120

Simha N, Fischer F, Shan G, Chene C, Kolednikf O (2008) J-integral and crack driving force in elastic-plastic materials. J Mech Phys Solids 56:2876–2895

Steinmann P (2000) Application of material forces to hyperelastostatic fracture mechanics. I. Continuum mechanical setting. Int J Solids Struct 37:7371–7391